GLOBEX: Wave dynamics on a shallow sloping beach

Hervé Michallet, B. Gerben Ruessink, Mariana Vieira Lima Matias da Rocha, Anouk de Bakker, Dominic A. van Der A, Andrea Ruju, Paulo A. Silva, Nadia Sénéchal, Vincent Marieu, Marion Tissier, et al.

GLOBEX: WAVE DYNAMICS ON A SHALLOW SLOPING BEACH

Hervé Michallet (1), Gerben Ruessink (2), Mariana V.L. Rocha (1,3), Anouk de Bakker (2), Dominic van der A (4), Andrea Ruju (5), Paulo A. Silva (3), Nadia Sénéchal (6), Vincent Marieu (6), Marion Tissier (2), Rafael Almar (7), Tiago Abreu (8), Florent Birrien (6), Laure Vignal (1), Eric Barthélemy (1), Dominique Mouazé (9), Rodrigo Cienfuegos (10) & Peter Wellens (11)

(1) LEGI, Univ. Grenoble, France, herve.michallet@legi.cnrs.fr
(2) Dept. Physical Geography, Faculty of Geosciences, Utrecht Univ., The Netherlands, b.g.ruessink@uu.nl
(3) CESAM & Department of Physics, University of Aveiro, Portugal. psilva@ua.pt
(4) School of Engineering, Univ. Aberdeen, Scotland. d.a.vandera@abdn.ac.uk
(5) Environmental Hydraulics Institute "IH Cantabria", Univ. Cantabria, Spain. andrea.ruju@unican.es
(6) EPOC, Univ. Bordeaux, France, n.senechal@epoc.u-bordeaux1.fr
(7) IRD, UMR LEGOS (CNRS/CNES/IRD/Univ. Toulouse), France. rafael.almar@ird.fr
(8) CESAM & Dep. of Civil Eng., Polytechnic Institute of Porto, Portugal. taa@isep.ipp.pt
(9) M2C, Univ. Caen, France. dominique.mouaze@unicaen.fr
(10) DIHA, Pontificia Universidad Católica de Chile, Chile. racienfu@ing.puc.cl
(11) Deltares, The Netherlands, peter.wellens@deltares.nl

As waves approach the shore, their non-linear dynamics becomes increasingly important. Most of our understanding of wave non-linearity has resulted from theoretical work, laboratory experiments and field studies on beaches slopes steeper than about 1:40. There, very strong non-linear processes happen locally and on a short time scale, as demonstrated by narrow surf zones with plunging or collapsing breakers. The non-linearity on gently-sloping beaches, typical of high-energy dissipative environments, has a different character, as it can build up over a long period of time and along an extensive cross-shore area. This contribution serves to introduce the GLOBEX project, during which a high-resolution (in space and time) data set of the cross-shore evolution of short and infragravity waves was collected on a low-sloping (1:80) non-mobile laboratory beach. As non-linear transfers also occur in the vertical from the free-stream flow downwards into the bottom boundary layer, additional flow measurements performed with Laser Doppler Anemometry are also briefly presented.

1. INTRODUCTION

Morphological change in the nearshore zone arises from the complex interplay of water motion, sediment transport, and the morphology itself. The governing water motion, predominantly short (2 – 15 s) waves and wave-induced processes, contains strongly non-linear aspects. This non-linearity is obvious from, for example, the increasingly non-sinusoidal shape of short waves as they approach the shore through the shoaling and breaking zone (e.g., Elgar and Guza, 1985), and the generation of infragravity waves (e.g., Herbers et al., 1994, 1995), oscillatory motions in the sea surface with periods of 20 to 200 s. The non-linearity in the water motion is crucial to sediment transport. Non-sinusoidal short waves are the dominant mechanism responsible for onshore sediment transport under mild weather conditions (e.g., O'Donoghue and Wright, 2004; Van der A et al., 2010; Ruessink et al., 2011) and may also contribute to off-shore transport (Ribberink and Al-Salem, 1994; Grasso et al., 2011). Infragravity waves can dominate the water motion close to the shore during more adverse weather (e.g., Guza and Thornton, 1982; Ruessink et al., 1998; Ruggiero et al., 2004; Sénéchal et al., 2011; De Bakker et al., 2014) and are important to beach and dune erosion (e.g., Russell, 1993; Van Thiel de Vries et al., 2008).

Wave non-linearity is of paramount importance on both steep and low-sloping beaches, but has different characteristics in each case. While on steep beaches very strong non-linear processes happen locally and on a short time scale (as demonstrated by narrow surf zones with plunging or collapsing breakers), the non-linearity on low-sloping beaches is significant because it builds up over a long

period of time along a cross-shore extensive area. This second case of strong non-linearity is not well documented; most of our understanding and predictive ability of nearshore processes have resulted from theoretical work, laboratory experiments, and field studies on beaches with slopes steeper than about 1:40. Within this context, a team including researchers from 9 European institutes in France, Spain, Portugal, United Kingdom and the Netherlands, as well as an institute from Chile, obtained funding in the framework of the Hydralab IV programme to perform the GLOBEX project – Gently sLOping Beach Experiment – in the 100-m long, small-scale Scheldegoot (Scheldt Wave Flume) of Deltares, Delft, The Netherlands.

The overall aim of the project was to collect a high-resolution (in space and time) data set of the cross-shore evolution of short and infragravity waves on a 1:80 concrete beach for a range of wave conditions, focusing on infragravity-wave dynamics, wave propagation, and boundary-layer dynamics. A detailed account of the GLOBEX project, including the description of the experimental set-up, the experimental programme, and the instrumentation used, has been presented at Coastal Dynamics 2013 (see Ruessink et al., 2013). A general overview of the cross-shore transformation of various wave properties was also provided. Additional preliminary results have been presented at Coastal Dynamics 2013 covering the various WPs in GLOBEX (Almar et al., 2013; De Bakker et al., 2013; Rocha et al., 2013; Ruju et al., 2013; Tissier et al., 2013; Van der A et al., 2013). In this paper, after recalling briefly the experimental procedure, we present various aspects of data processing applied on a bichromatic wave condition.

2. METHODS

2.1. *Experimental set-up*

The laboratory experiments were performed in the Scheldegoot (Scheldt Wave Flume) of Deltares, Delft, The Netherlands in April 2012. The flume is 110 m long, 1 m wide and 1.2 m high; it has glass windows along most of its length. The waves were generated with a piston-type wave maker equipped with Active Reflection Compensation (ARC) to minimize reflections from the wave paddle. An impermeable concrete beach with a 1:80 slope was constructed, with its toe at 16.57 m from the wave maker (in rest position, x = 0 m), see Figure 1. All experiments were run with a still water depth of 0.85 m over the horizontal section; this implies that the still-water shoreline was at x = 84.57 m. The material that was laying loose on the concrete bed before the flume was filled with water had a median grain size D50 of 0.75 mm; D10 and D90 amounted to 0.49 and 1.15 mm, respectively.

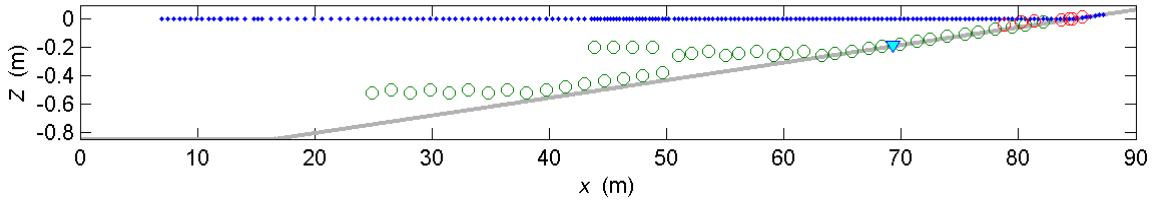

Figure 1. Bed elevation Z versus cross-shore distance x in the Scheldegoot during the GLOBEX project. Here, x = 0 is the wave-maker location, while Z = 0 corresponds to the still water level. The symbols indicate the location of the measurements used in this paper: the 190 dots are the positions of the wave gauges; the green (red) circles are the positions and heights above the bed of the EMCMs (ADV); the triangle is the location of the LDA. The bed level was determined with a terrestrial laser scanner before the flume was filled with water.

2.2. *Experimental programme*

The programme comprised 8 wave conditions grouped in 3 test series with varying complexity (Table 1). All wave-paddle steering signals in Series A and B were made with second-order wave generation. In Series A, the signals were based on a JONSWAP spectrum with a peak enhancement factor γ of 3.3 for A1 and A2, and of 20 for A3 to provide a narrow-banded (in frequency) spectrum for the swell waves. The bichromatic frequencies in Series B were chosen in order to get the same waves in each wave-packet (6 waves per packet for B1, 10 waves per packet for B2 and B3). The packets of

condition B3 had a larger modulation compared to that of B1 and B2. Since the wave height and steepness were small, the use of first-order wave generation was considered adequate for C1. The signals of A and B had a total duration of 75 minutes; the signal of C1 was 30 minutes long.

Table 1. Overview of wave conditions

Test series A					
	H_s (m)	T_p (s)			Remark
A1	0.10	1.58			JONSWAP, γ=3.3; prototype: H_s = 2 m; T_p = 7 s
A2	0.20	2.25			JONSWAP, γ=3.3; prototype: H_s = 4 m; T_p = 10 s
A3	0.10	2.25			JONSWAP, γ=20; prototype: H_s = 2 m; T_p = 10 s
Test Series B					
	a_1 (m)	a_2 (m)	f_1 (Hz)	f_2 (Hz)	Remark
B1	0.09	0.01	6/15	7/15	$1/(f_2-f_1)$ = 15 s; $(f_1+f_2)/2$ = 0.433 Hz
B2	0.09	0.01	0.42	0.462	$1/(f_2-f_1)$ = 23.81 s; $(f_1+f_2)/2$ = 0.441 Hz
B3	0.07	0.03	0.42	0.462	$1/(f_2-f_1)$ = 23.81 s; $(f_1+f_2)/2$ = 0.441 Hz
Test Series C					
	H (m)	T (s)			Remark
C1	0.02	23.8			
C2	0.20	2.25			Ran for the wave bottom boundary layer study only

2.3. *Instruments and measurements*

A wide suite of instruments was deployed during the experiments:

- **Waves** – Water-surface elevation and flow velocities were measured using 21 wave gauges (WGs) and 5 electromagnetic current meters (EMCMs) mounted on movable trolleys. All data from the WGs and EMCMs were collected at 128 Hz. The height of the EMCMs above the bed varied between 0.01 m and 0.3 m, depending on the location within the flume (see Figure 1). In addition, the water-surface elevation was also imaged at 20 Hz using 2 video cameras looking sideways through the glass windows and one video camera looking obliquely from above.
- **Swash** – Instruments focusing specifically on swash motions comprised a single downward-looking video camera (sampling at 20 Hz), a swash-wire mounted at about 1cm above the bed (sampling at 128 Hz), a RIEGL VZ-400 terrestrial laser scanner, and an acoustic Doppler velocimeter (ADV).
- **Boundary-layer dynamics** – Equipment to measure horizontal and vertical velocities inside the wave bottom boundary layer comprised a Deltares Laser Doppler Velocimeter (LDV) and a Dantec Laser Dopper Anemometry (LDA) system at x = 60.6 m and x = 69.3 m, respectively. Only results from the LDA system are presented here. The vertical translation precision of the LDA was 0.05 mm. The output of a WG not included in the aforementioned 21 WGs was used to measure sea-surface elevation at the location of the LDA. Silver-coated hollow-glass spheres with a diameter of 10 μm were used to seed the flow, except during the first few days of the experiment when seeding material was unavailable.

3. PRELIMINARY RESULTS

Various results were discussed in De Bakker et al. (2013) on infragravity-wave dissipation; Rocha et al. (2013) on non-linearity of short and long waves; Almar et al. (2013) and Tissier et al. (2013) on short-wave celerity; Van der A et al. (2013) on wave boundary layer dynamics; and Ruju et al. (2013) on swash motions. Here, measurements obtained with the WGs and EMCMs are used to provide some features of the observed cross-shore evolution of the short and infragravity waves in series B3. In addition, boundary layer measurements for the same wave condition will be shown in section 3.4.

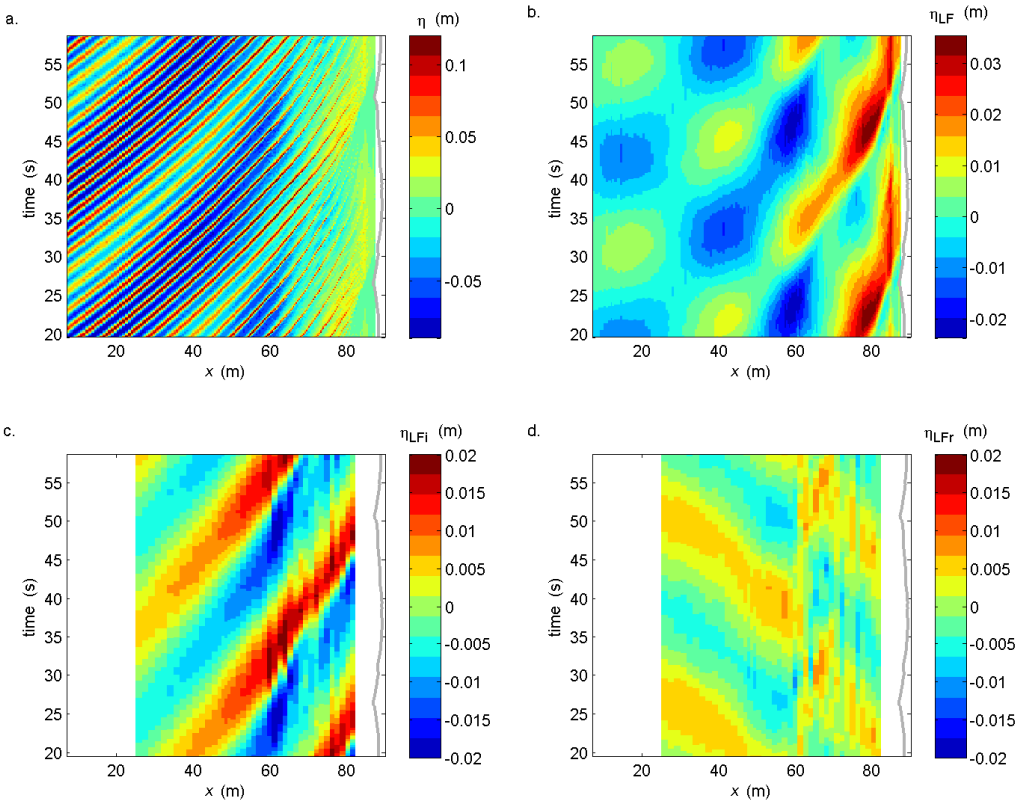

Figure 2. Forty-second time-space diagram of the free-surface elevation measured by the wave gauges during condition B3: total signal (a), low-pass filtered (b), incoming (c), and reflected (d) low-frequency waves. Warm (red) colours correspond to values above 0 (the still water level), cold (blue) colours to values below 0.The gray line fluctuating around $x \sim 87$ m is the shore-line determined with the swash wire.

3.1 *Short and long wave propagation*

Figure 2a shows a 40-second long time-space diagram of the free-surface elevation of condition B3, together with the approximate location of the uprush and backwash motion as determined with the swash wire. The low-pass filtered (cut-off at $(f_1+f_2)/4$) signal shown in Figure 2b exhibits a low-frequency standing-wave pattern. Following Guza and Thornton (1982), incoming and reflected waves are deduced from the analysis of co-located WGs and EMCMs (Figure 2c, d). The separation method is likely only qualitative in both breaking ($x \sim 60$ m) and surf zones, but it nevertheless gives a good indication of the long-wave propagation. The reflected long-wave energy at the toe of the slope is of the same order of that of the incoming bound long wave, for this high-groupiness bichromatic case. This is in marked contrast with the A series for which most of the incoming infragravity-wave energy is dissipated at the beach (see De Bakker et al., 2013).

Time-series of the free-surface elevation at the first gauge (x = 6.96 m), at the breaking point (x = 63.58 m), in the innermost part of the surf zone and in the swash zone are plotted in Figure 3. The low-frequency modulation of 23.8 s period is seen to evolve along the beach, developing a distinct saw-tooth shape in the inner surf zone. The short waves riding the long-wave crests are travelling faster than the short-wave crests in the long-wave troughs, due to the water-depth modulation. The bore formation mechanism is thus illustrated as short waves piling up at the long-wave front (see also Tissier et al., 2013). Subsequent long-wave dissipation is likely induced by breaking at the steep front (Van Dongeren et al., 2007).

The wave spectrum evolution along the beach is shown in Figure 4. Before reaching the sloping part (at x = 16.57 m), the wave energy is mainly concentrated in the two first-order components of the bichromatic, f_1 and f_2, and in three second-order terms: the bound long wave at (f_2-f_1) and the higher harmonics $(2f_1)$ and (f_1+f_2). During shoaling, the energy of higher-order harmonics increases: $(2f_1-f_2)$

and ($2f_2$-f_1) first, then ($3f_1$-f_2), ($3f_1$) and ($2f_1$+f_2). These are produced by interactions between first- and second-order waves (Elgar and Guza, 1985). Higher-order harmonics become increasingly important before the break point (x ~ 60 m). In the breaking zone, the main components are the first to lose their energy. Notably, in the inner surf zone (x ~ 75 m), high-order harmonics tend to dominate first-order ones.

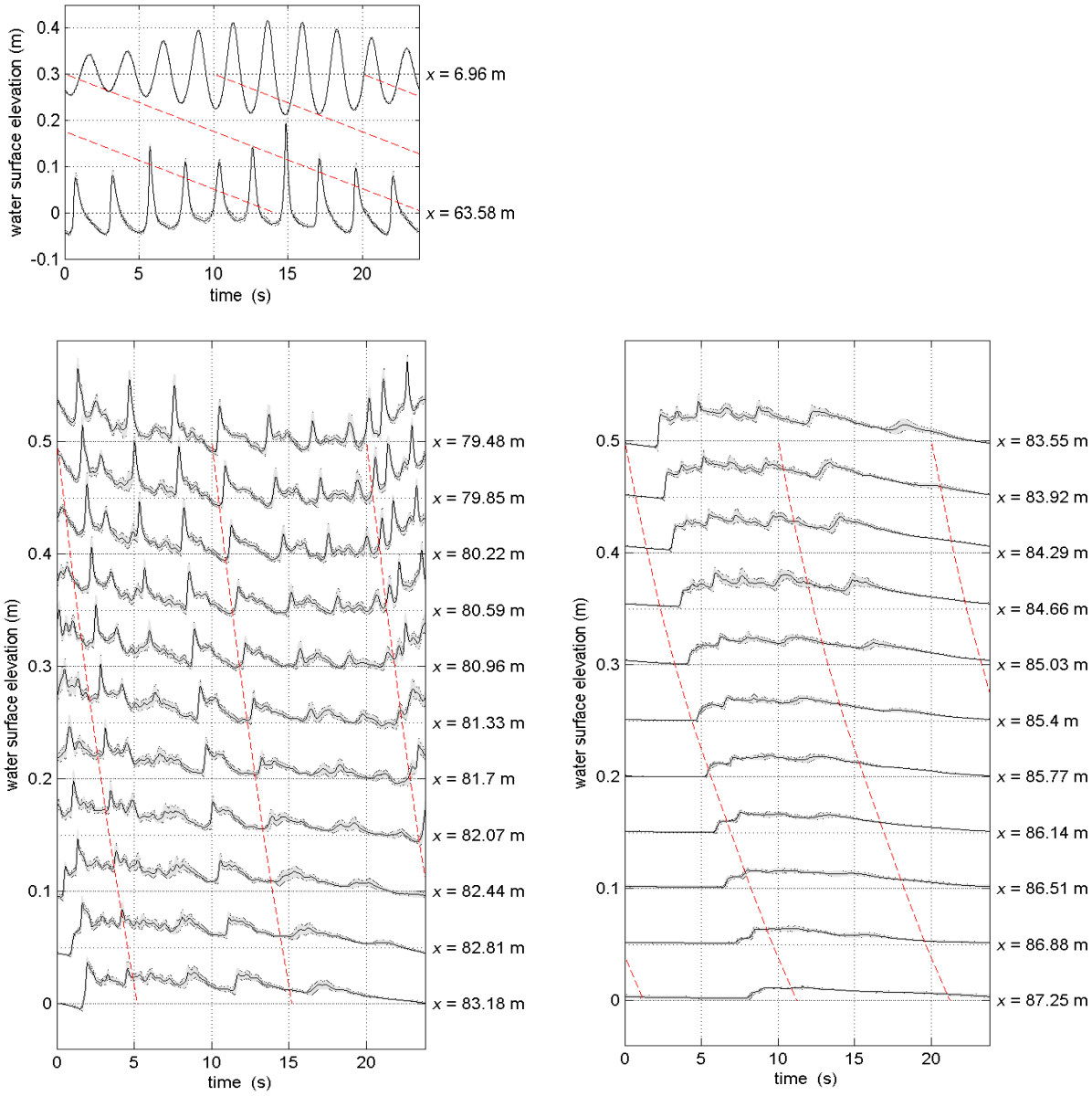

Figure 3. Free-surface elevation of the wave group at various cross-shore positions: black lines are ensemble average over 173 groups and the gray shading indicates the standard deviation. The red lines show the propagation at the linear wave speed.

3.2 *Comparison with numerical modeling*

One of the aims of the project is to provide a data set that can be used for comparison with numerical models. Ruju et al. (2014) have presented SWASH numerical results focusing on run-up oscillations for the A series. The Boussinesq-type Serr1D model (Cienfuegos et al., 2006, 2007) has been shown to reproduce correctly wave non-linearities for random waves over complex beach topographies (Michallet et al., 2011). Here it is used for comparison with case B3.

Time-series in the breaking, inner surf and swash zones are shown in Figure 5. The overall bore formation is correctly reproduced by the model. The short wave phases are well captured in the surf

zone while discrepancies in height may appear for individual waves, leading to larger differences in the swash zone. Noteworthy, the computed velocities in the swash zone compare well with the ADV measurements when the water depth is larger than 1 cm.

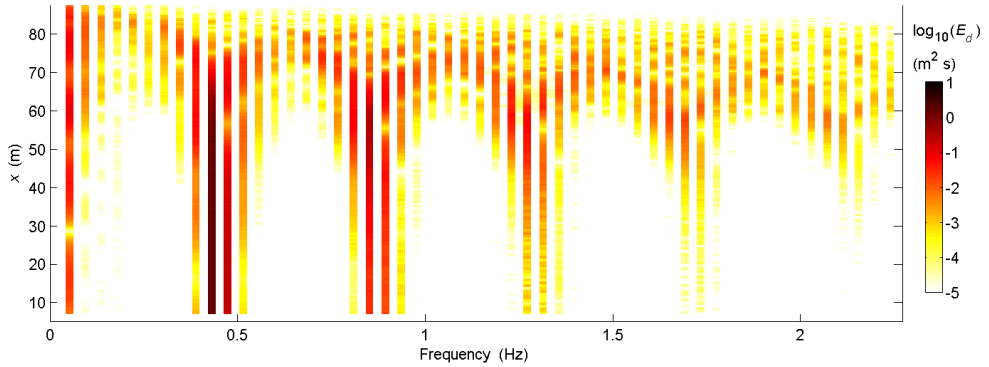

Figure 4. Logarithm of energy density E_d as a function of frequency f and cross-shore position x for condition B3. The energy is concentrated at the multiples of (f_2-f_1) for which the lines have been thickened into stripes for readability.

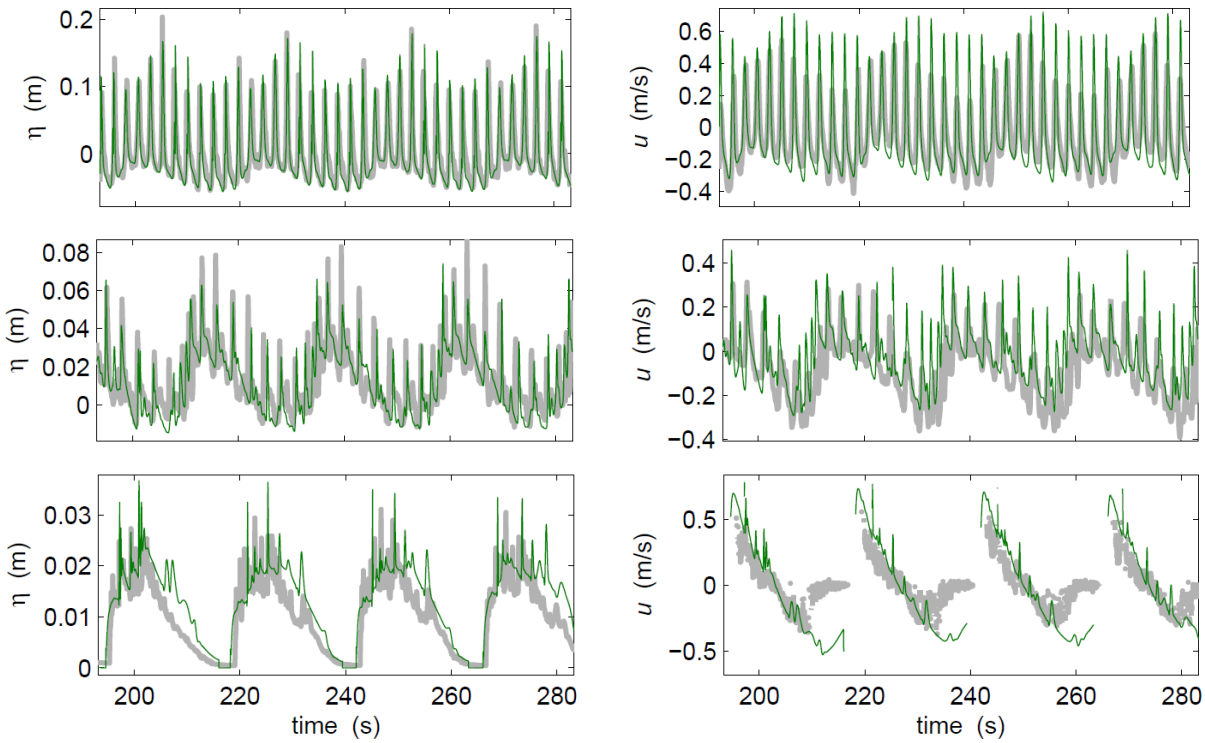

Figure 5. Time series of surface elevation (left) and velocities (right) in (from top to bottom) the breaking (x = 63.2 m), inner surf (x = 79.5 m) and swash zones (x = 85.4 m): model results (green lines) vs measurements (grey dots). Model velocities are depth integrated while velocities were measured 1 cm above the bed.

Serr1D relies on several parameters for computing breaking inception and further dissipation (see Cienfuegos et al., 2010). The cross-shore evolution of statistical quantities is plotted for two different sets of parameters in Figure 6. The model is easily reproducing some general trends, including set-down and set-up, breaking location, overall energy decay, long wave build-up, dissipation and reflection. In particular, the standard deviation of the low-pass filtered signals exhibits a standing-wave pattern with nodes close to zero, thus confirming that the reflected free long wave has about the same amplitude as the incoming bound long wave in this case.

The wave skewness and asymmetry in the surf zone are more sensitive to the choice of the parameters, such as the limiting front slope for breaking initiation and termination. This emphasizes that a good description of individual wave breaking is crucial for reproducing a correct phasing of the short-wave crests (see bottom of Figure 5) that may thus influence wave non-linearity variations (see the four bottom plots in Figure 6). This also highlights the need for investigating further the individual wave propagation characteristics, including a correct description of the individual wave celerity (Tissier et al., 2011; 2013).

As shown on the right side of Figure 6, the trends for depth-integrated velocities computed by the model are similar to those of the velocities measured at one depth (close to the bed in general, see Figure 1). Noteworthy, the experimental data of the mean velocity are very scattered (top-right in Figure 6). (Not shown here, the mean cross-shore velocities are much less scattered for the random wave cases.) This scatter might be attributed to the presence of secondary motions generated by the transverse waves observed for series B (see also the discussion in Van der A et al., 2013). These spurious waves are likely generated at the break point, at a depth ($h_b \approx 0.35$ m) where the transverse mode-1seiching can be excited at frequency (f_1+f_2).

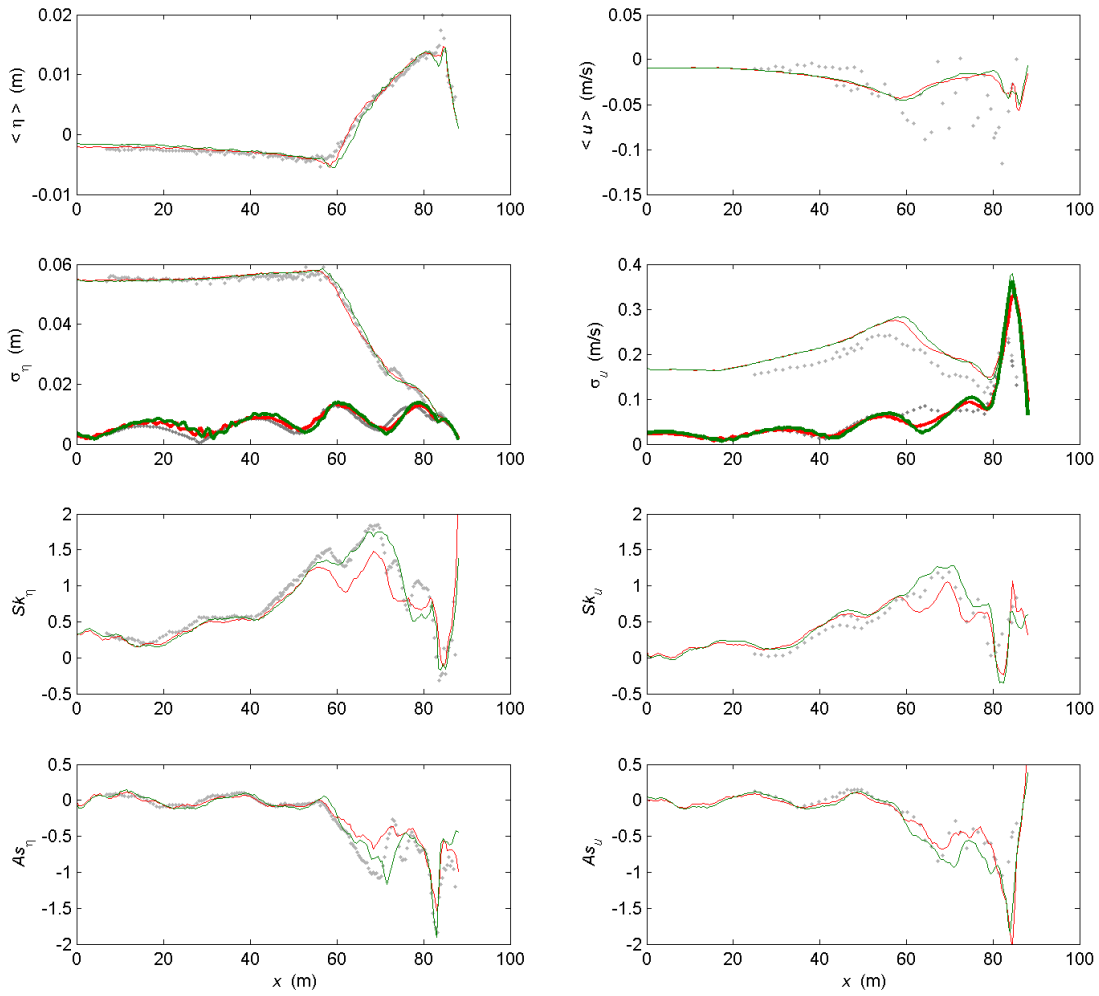

Figure 6. Cross-shore variation of statistical quantities for surface displacement (left) and velocities (right): measurements (dots) vs Serr1D results for two sets of breaking parameters (red and green lines). From top to bottom: mean, standard deviation (low-pass filtered are darker dots and thicker lines), skewness, asymmetry.

3.3 *Bispectral analysis*

In order to better understand the cross-shore evolution of the wave non-linear properties, a bispectrum analysis was conducted. The method is described in Elgar and Guza (1985) and is not recalled here. It

is aimed at finding the three-wave couplings defined by frequency triads (f_m, f_n, f_m+f_n) with $n \leq m$. The sum over all triads of the real (imaginary) part of the bispectrum is equal to the wave skewness (asymmetry). The components that constitute wave skewness at four cross-shore locations are shown in Figure 7 along with the wave spectrum and the rate of dissipation of the Fourier components. Largely positive (hot colors) or negative (cold) values of $Sk_{m,n}$ indicate strong triad interactions, while hot (cold) colors in the top panels indicate gain (loss) of energy.

In the shoaling zone (Figure 7a), the triad at (m=10, n=10) corresponding to (f_1, f_1, $2f_1$) is the main constituent of the wave skewness, with noticeable secondary positive contributions at (f_2, f_1, f_1+ f_2) and ($2f_1$, f_1, $3f_1$) and a negative contribution at (f_1, f_2- f_1, f_2). In terms of spectral evolution, the main feature seen at this stage is a decay of the main components f_1 and f_2 and an increase of the higher harmonics $2f_1$ and $3f_1$.

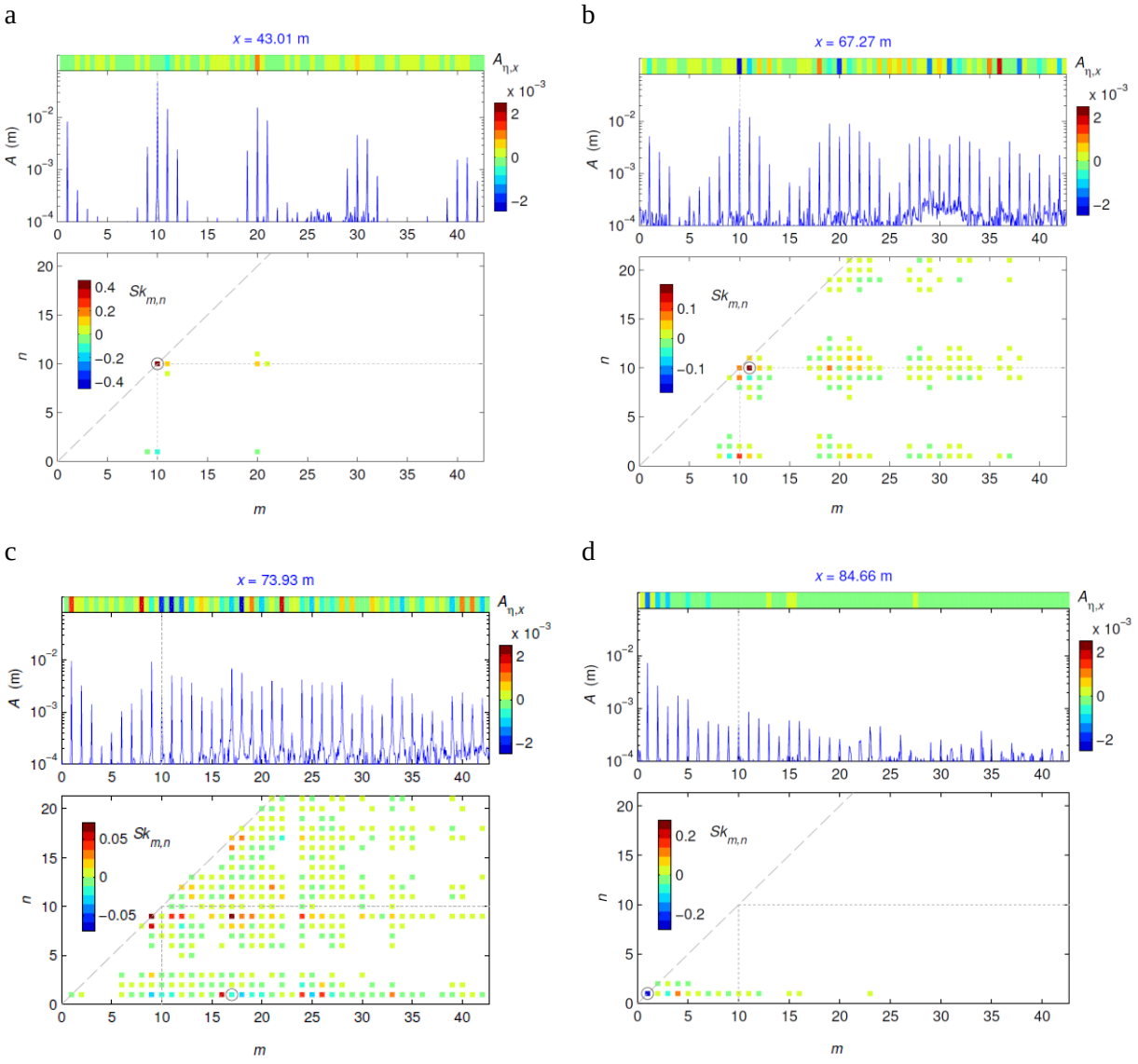

Figure 7. Spectral and bispectral analysis at four cross-shore locations: shoaling (a), outer surf (b), inner surf (c), and swash (d) zones. In each panel: (top) amplitude of the Fourier components (solid line) and their variations with x (in color) against $m = f_m/(f_2\text{-}f_1)$ and (bottom) real part of the bispectrum against m and n, where $n = f_n/(f_2\text{-}f_1)$ with (f_m, f_n, f_m+f_n) the frequency triad considered (only triads with large both bicoherence and bispectrum amplitude are shown). Note that, for the present case B3, $f_1/(f_2\text{-}f_1)$=10 and $f_2/(f_2\text{-}f_1)$=11.

After the break point, the number of triads contributing to *Sk* considerably increases as shown in Figure 7b. The main bispectrum component (circled) is now at (f_2, f_1, f_1+f_2), although it still represents less than 10% of the total *Sk* at this stage (*Sk* = 1.8 at x = 67 m in Figure 6). The outer surf zone is also characterized by an energy decay of the main frequency components (e.g. f_1, f_2, $2f_1$). A notable energy increase that is not linked to any triad interaction is seen at frequencies corresponding to m = 25 and 35. The energy transfer to these frequencies is thus likely due to four-wave interactions. In the inner surf zone (Figure 7c) most of the wave components are efficiently interacting, with the prevalence of interactions involving low-frequency waves at n < 10, i.e. with at least one of the frequencies of each triad being smaller than f_1. The peaks in the spectrum are more evenly distributed in the high-frequency domain (m > 10) and a notable energy increase in the low-frequency range is observed at m = 1 and m = 8. Finally, interactions involving only low-frequency waves (m+n < 10) are prevailing in the swash zone (Figure 7d), and the main peaks at m = 1, 2, 3 are seen to lose their energy.

As an attempt to summarize these observations, the frequency domain is separated into several sub-domains. The contributions of the different triads are integrated over each of these sub-domains. Figure 8a illustrates that the contribution to wave-height of frequencies larger than f_2 increases in the shoaling zone and becomes, in the inner surf and swash zones (x > 70 m), larger than that of frequencies f_1 and f_2. The low-frequency contribution shows again a standing-wave pattern and tends to dominate other contributions in the innermost surf zone. Figures 8b,c indicate that the reflected long wave modulates the low-frequency contribution to non-linearities. Interactions involving only long waves dominate for x > 80 m. As shown in Figure 8d, most of the triad interactions have a negative biphase after breaking (x > 60 m), which means energy is being transferred to higher frequencies, with the notable exception of interactions involving triads with only long-waves , for which the biphase drops sharply to negative only closer to the coast, at x = 77 m. This position might be thought as the boundary after which all wave components are breaking.

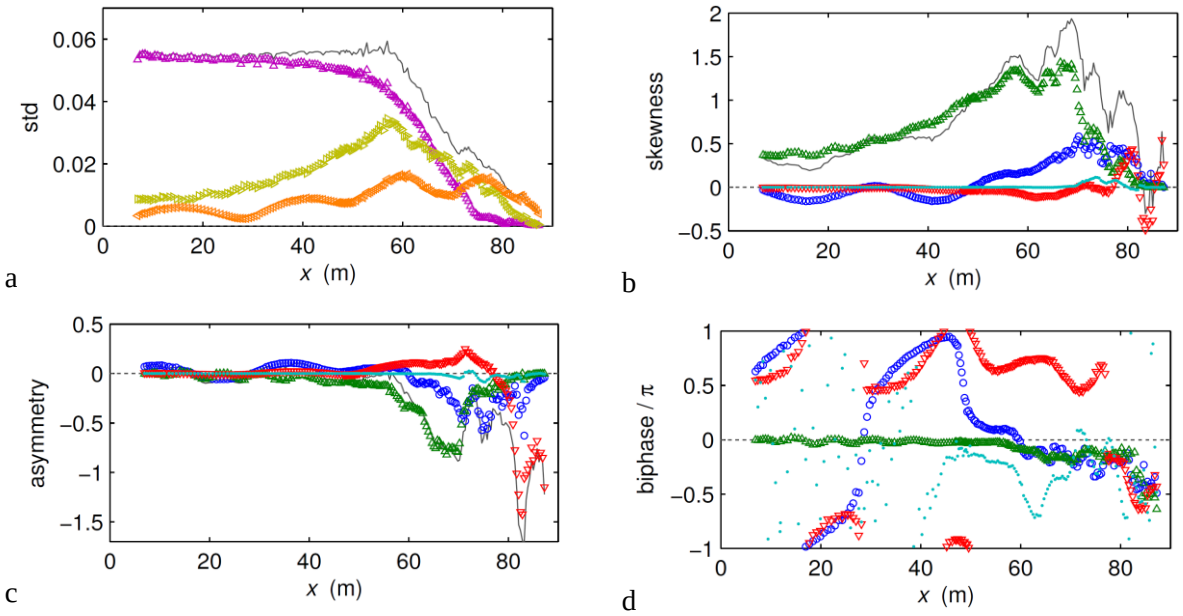

Figure 8. (a) Standard deviation of free surface elevation (solid line), rms of Fourier (magenta) main components f_1 and f_2, (yellow) components larger than f_2, (orange) components smaller than f_1. (b) Wave skewness (solid line), sum of the real part of the bispectrum of triads involving (blue) only one low frequency ($f_m \geq f_1$, $f_n < f_1$, f_m+f_n), (green) only high frequencies ($f_m \geq f_1$, $f_n \geq f_1$, f_m+f_n), (red) only low frequencies ($f_m < f_1$, $f_n < f_1$, f_m+$f_n < f_1$), (light blue) two low frequencies and one high frequency ($f_m < f_1$, $f_n < f_1$, f_m+$f_n \geq f_1$). (c) Same as in (b) for the wave asymmetry. (d) Corresponding averaged biphase.

3.4 *Bottom boundary layer measurements*

The procedure used for the study of the boundary layer has been extensively presented in Van der A et al. (2013), along with the estimation of the bed roughness and results on the vertical variation of wave non-linear parameters. As an example, Figure 9f shows for the B3 wave group that the asymmetry

observed outside the boundary layer is transferred into skewness close to the bed. This is a key process for explaining how steep-front waves may promote sediment transport (Henderson et al., 2004; Abreu et al., 2013; Berni et al., 2013).

As the reproduction of identical bichromatic wave groups was achieved, the turbulent velocity fluctuations can be extracted through ensemble averaging, as shown by the density spectra in Figure 9a,b. Since most of the peaks at the main frequencies (around 0.4 Hz) disappear through the procedure, low-frequency variations are notable, particularly outside the boundary layer at z = 10 mm. The vertical profiles of the fluctuations are shown in Figure 9d. While the magnitude of the vertical component is relatively uniform over the 1-cm range investigated, the horizontal component tends to decrease towards the bed. Noteworthy, the standard deviation of the horizontal velocity follows a log-law trend for elevations in the range 0.3 – 1 mm (Figure 9c). The measurements in the first 0.3 mm above the bed are likely affected by local roughness. Finally, Figure 9e illustrates the on-shore mean current known as boundary-layer streaming (Longuet-Higgins, 1953; Yu et al., 2010; Kranenburg et al., 2013).

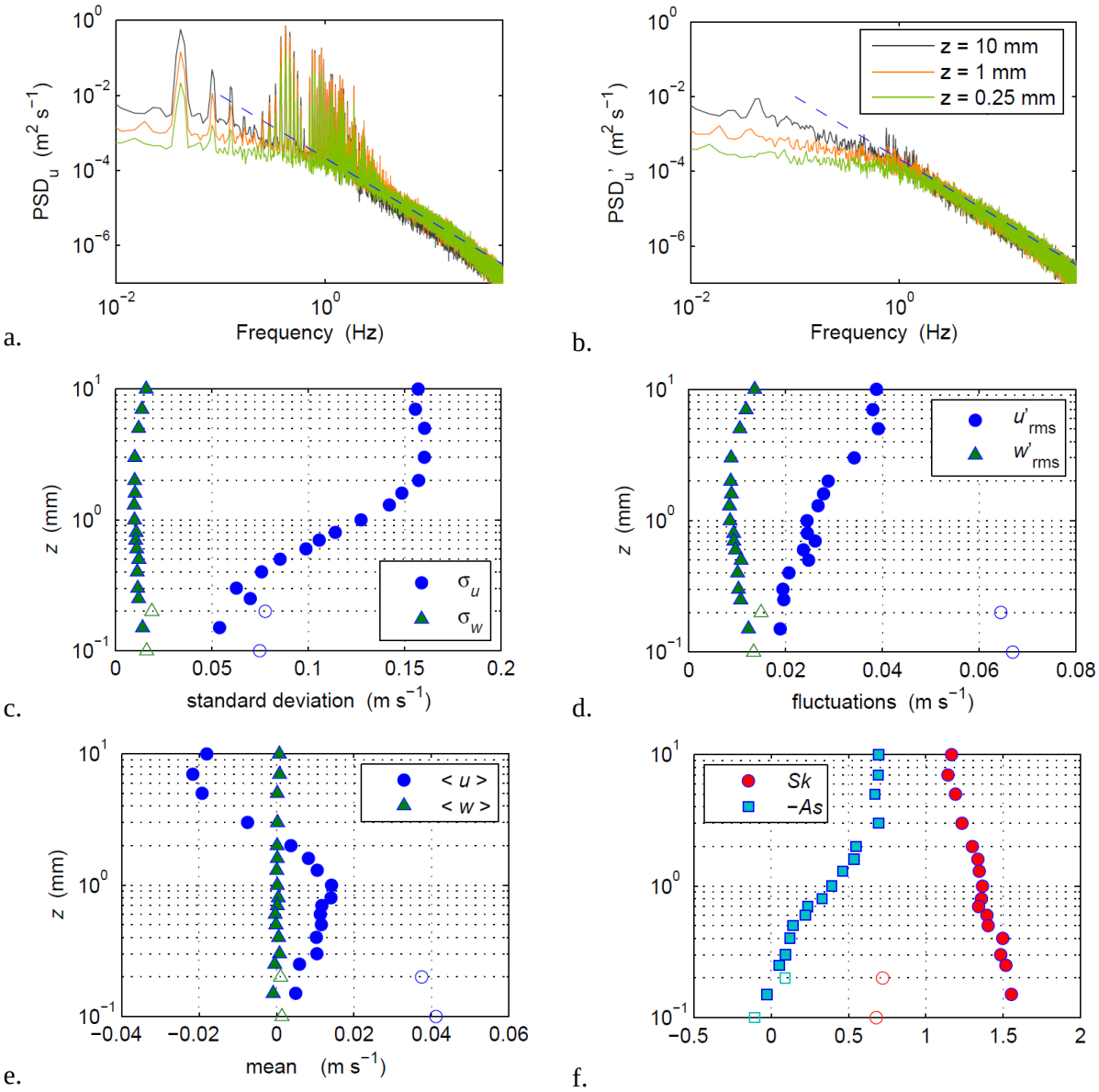

Figure 9. Example of boundary-layer measurements: (a) spectral density of horizontal velocities at three elevations above the bed and (b) with the ensemble average signal removed (the dashed line is the -5/3 slope); vertical profiles of: (c) standard deviation of horizontal and vertical velocities, (d) their fluctuations, (e) mean values; (f) skewness and asymmetry of u. The blank symbols stand for measurements made without seeding material.

4. CONCLUSION

The GLOBEX experiment took place over an approximately 1 month period in April 2012. Almost 25 scientists from 10 institutes were involved, and 13 staff from Deltares performed technical support. The experiments resulted in a highly detailed data set of the cross-shore evolution of short and infragravity waves from well seaward of the surf zone up to and including the leading edge of the swash motion on a fixed 1:80 sloping beach. In addition, high-resolution observations of the horizontal and vertical flow in the wave bottom boundary layer were collected. Examples of data analysis were briefly presented here for a single bichromatic wave condition with the aim of illustrating the wealth of processes that can be studied with the GLOBEX data set.

ACKNOWLEDGEMENT

We are greatly indebted to the Deltares technicians and staff members (Frank van Eeden, John Coolegem, Pieter Pasterkamp, Frans de Vreede, Richard Boele, Rob Hoffman, Jaap de Schipper, Paul Meys, Job Waaijerink, Hans Deutekom, Jelle Molenaar, Ivo Wenneker and Irv Elshoff) for their excellent support during the experiments. It was a pleasure to work with you! We also wish to thank all other GLOBEX team members (Céline Berni, Marcel van Maarseveen, Philippe Bonneton, Javier L. Lara, Giovanni Coco, and Iñigo Losada Rodriguez) for their help in preparing the original proposal or collecting the GLOBEX data set, and for making the stay in Delft such a pleasant and memorable occasion. This work has been supported by European Community's Seventh Framework Programme through the grant to the budget of the Integrating Activity HYDRALAB IV within the Transnational Access Activities, Contract no. 261520.

REFERENCES

Abreu, T., Michallet, H., Silva, P.A., Sancho, F., Van der A, D. and Ruessink, B.G., 2013. Bed shear stress under skewed and asymmetric oscillatory flows. *Coastal Engineering*, 73: 1-10.

Almar, R., Bonneton, P., Michallet, H., Cienfuegos, R., Ruessink, G. and Tissier, M., 2013. On the use of the Radon transform in studying wave dynamics. *Proceedings Coastal Dynamics* 2013.

Berni, C., Barthélemy, E. and Michallet, H., 2013. Surf zone cross-shore boundary layer velocity asymmetry and skewness: an experimental study on a mobile bed. *Journal of Geophysical Research Oceans*, *118*, 2188–2200.

Cienfuegos, R., Barthélemy, E., and Bonneton, P., 2006. A fourth-order compact finite volume scheme for fully nonlinear and weakly dispersive Boussinesq-type equations. Part I: model development and analysis, *Internat. J. Numer. Methods Fluids,* 51(11), 1217–1253.

Cienfuegos, R., Barthélemy, E., and Bonneton, P., 2007. A fourth-order compact finite volume scheme for fully nonlinear and weakly dispersive Boussinesq-type equations. Part II: boundary conditions and validation, *Internat. J. Numer. Methods Fluids,* 53(9), 1423–1455.

Cienfuegos, R., Barthélemy, E., and Bonneton, P., 2010. A wave-breaking model for Boussinesq-type equations including roller effects in the mass conservation equation, *J. Waterw. Port Coastal Ocean Eng.,* 136(1), 10–26.

De Bakker, A., Tissier, M., Marieu, V., Sénéchal, N., Ruju, A., Lara, J. and Ruessink, G., 2013. Infragravity-wave dissipation on a low-sloping beach. *Proceedings Coastal Dynamics* 2013.

De Bakker, A.T.M., Tissier, M.F.S. and Ruessink, B.G., 2014. Shoreline dissipation of infragravity waves. *Continental Shelf Research.*

Elgar, S. and Guza, R.T., 1985. Observations of bispectra of shoaling surface gravity waves. *Journal of Fluid Mechanics*, 161: 425-448.

Grasso, F., H. Michallet, and E. Barthélemy (2011), Sediment transport associated with morphological beach changes forced by irregular asymmetric, skewed waves, *J. Geophys. Res*., 116, C03020.

Guza, R.T. and Thornton, E.B., 1982. Swash oscillations on a natural beach. *Journal of Geophysical Research*, 87: 483-491.

Henderson, S.M., Allen, J.S., Newberger, P.A., 2004. Nearshore sandbar migration predicted by an eddy-diffusivity boundary layer model. *Journal of Geophysical Research,* 109(C06024).

Henderson, S.M., Guza, R.T., Elgar, S., Herbers, T.H.C. and Bowen, A.J., 2006. Nonlinear generation and loss of infragravity wave energy. *Journal of Geophysical Research*, 111, doi:10.1029/2006JC003539.

Herbers, T.H.C., Elgar, S. and Guza, R.T., 1994. Infragravity-frequency (0.005-0.05 Hz) motions on the shelf. Part I: Forced waves. *Journal of Physical Oceanography*, 24: 917-927.

Herbers, T.H.C., Elgar, S., Guza, R.T. and O'Reilly, W.C., 1995. Infragravity-frequency (0.005-0.05

Hz) motions on the shelf. Part II: Free waves. *Journal of Physical Oceanography*, 24: 917-927.
Kranenburg, W.M., Ribberink, J.S., Schretlen, J.J.L.M., Uittenboogaard, R.E., 2013. Sand transport beneath waves: The role of progressive wave streaming and other free surface effects. *Journal of Geophysical Research*, 118, 1-18.
Lara, J.L., Ruju, A. and Losada, I.J., 2010. Reynolds averaged Navier-Stokes modelling of long waves induced by a transient wave group on a beach. *Proceedings of the Royal Society A*, doi:10.1098/rspa.2010.0331.
Longuet-Higgins, M.S., 1953. Mass transport in water waves. *Philos. Trans. R. Soc. London Ser. A.,* 245, 531-581.
Michallet, H., Cienfuegos, R., Barthélemy, E. and Grasso, F. (2011). Kinematics of waves propagating and breaking on a barred beach. *European Journal of Mechanics B/Fluids*, **30**(6): 624-634
O'Donoghue, T. and Wright, S., 2004. Flow tunnel measurements of velocities and sand flux in oscillatory sheet flow for well-sorted and graded sands. *Coastal Engineering*, 51: 1163-1184.
Ribberink, J.S. and Al-Salem, A.A.,1994. Sediment transport in oscillatory boundary layers in cases of rippled beds and sheet flow. *Journal of Geophysical Research*, 99: 12707-12727.
Rocha, M., Silva, P.A., Michallet, H., Abreu, T. and Barthélemy, E., 2013. Nonlinearities of short and long waves across the shoaling, surf and swash zones: large-scale physical model results. *Proceedings Coastal Dynamics* 2013.
Ruessink, B.G., Kleinhans, M.G. and Van den Beukel, P.G.L., 1998. Observations of swash under highly dissipative conditions. *Journal of Geophysical Research*, 130: 3111-3118.
Ruessink, B.G., Michallet, H., Abreu, T., Sancho, F., Van der A, D.A., Van der Werf, J.J. and Silva, P.A., 2011. Observations of velocities, sand concentrations, and fluxes under velocity-asymmetric oscillatory flows. *Journal of Geophysical Research*, 116: doi:10.1029/2010JC006443.
Ruessink, B.G., Boers, M., Van Geer, P.F.C., De Bakker, A.T.M., Pieterse, A., Grasso, F. and De Winter, R.C., 2012. Towards a process-based model to predict dune erosion along the Dutch coast. *Netherlands Journal of Geosciences*, 91: 357-372.
Ruessink, B.G., Michallet, H., Bonneton, P., Mouazé, D., Lara, J., Silva, P.A., Wellens, P., 2013. GLOBEX: Wave dynamics on a gently sloping laboratory beach. *Proceedings Coastal Dynamics 2013.*
Ruggiero, P., Holman, R.A. and Beach, R.A., 2004. Wave run-up on a high-energy dissipative beach. *Journal of Geophysical Research*, 109: doi.10.1029/2003JC002160.
Ruju, A., Lara, J.L., Michallet, H., Sénéchal, N. and Losada, I.J., 2013. Transient swash motions on a gently sloping beach. *Proceedings Coastal Dynamics* 2013.
Ruju, A., Lara, J.L. and Losada, I.J., 2014. Numerical analysis of run-up oscillations under dissipative conditions. *Coastal Engineering*, 86: 45-56..
Russell, P., 1993. Mechanisms for beach erosion during storms. *Continental Shelf Research*, 13: 1243-1265.
Sénéchal, N., Coco, G., Bryan, K.R. and Holman, R.A., 2011. Wave runup during extreme storm conditions. *Journal of Geophysical Research*, 116: doi:10.1029/2010JC006819.
Tissier, M., Bonneton, P., Almar, R., Castelle, B., Bonneton, N., and Nahon, A., 2011. Field measurements and nonlinear prediction of wave celerity in the surf zone. *European Journal of Mechanics-B/Fluids*, 30: 635-641.
Tissier, M., Almar, R., Bonneton, P., Michallet, H., De Bakker, A. and Ruessink, G., 2013. Role of short and long-wave interaction on wave celerity in the surf zone of a low-sloping beach. *Proceedings Coastal Dynamics* 2013.
Van der A, D.A., O'Donoghue, T. and Ribberink, J.S., 2010. Measurements of sheet flow transport in acceleration-skewed oscillatory flow and comparison with practical formulations. *Coastal Engineering*, 57: 331-342.
Van der A, D.A., Mouazé, D., Vignal, L., Silva, P., Abreu, T., Barthélemy, E. and Michallet, H., 2013. Wave boundary layer dynamics on a low sloping laboratory beach. *Proceedings Coastal Dynamics* 2013.
Van Dongeren, A.R., Battjes, J., Janssen, T.T., Van Noorloos, J., Steenhauer, K., Steenbergen, G. and Reniers, A., 2007. Shoaling and shoreline dissipation of low-frequency waves. *Journal of Geophysical Research*, 112: doi:10.1029/2006JC003701.
Van Thiel de Vries, J.S.M., Van Gent, M.R.A., Walstra, D.J.R. and Reniers, A.J.H.M., 2008. Analysis of dune erosion processes in large-scale flume experiments. *Coastal Engineering*, 55: 1028-1040.
Yu, X., Hsu, T.J. and Hanes, D.M., 2010. Sediment transport under wave groups: relative importance between nonlinear wave shape and nonlinear boundary layer streaming. *Journal of Geophysical Research*, 115: doi:10.1029/2009JC005348.